ChemPubSoc Europe

DOI: 10.1002/cplu.201900568

CHEMPLUSCHEM Full Papers

In Situ Methylation Transforms Aggregation-Caused Quenching into Aggregation-Induced Emission: Functional Porous Silsesquioxane-Based Composites with Enhanced Near-Infrared Emission

Yehao Yan,[a] Richard M. Laine,[b] and Hongzhi Liu*[a]

Methylation of TPA-DCM (2-(2,6-bis-4-(diphenylamino)stryryl-4H-pyranylidene)malononitrile) that exhibits aggregation-caused quenching (ACQ) results in the fluorophore M-TPA-DCM (2-(2,6-bis((E)-4-(di-*p*-tolylamino)-styryl)-4H-pyran-4-ylidene]malononitrile) that shows aggregation-induced emission (AIE) and NIR fluorescence and has a conjugated "D-π-A-π-D" electronic configuration. Friedel-Crafts reaction of TPA-DCM and octavinylsilsesquioxane (OVS) resulted in a family of porous materials (TPAIEs) that contain the M-TPA-DCM motif and show large Stokes shifts (180 nm), NIR emission (670 nm), tunable porosity (S_{BET} from 160 to 720 $m^2 g^{-1}$, pore volumes of 0.13–0.55 $cm^3 g^{-1}$), as well as high thermal stability (400 °C, 5% mass loss, N_2). As a simple test case, one of TPAIE materials was used to sense Ru^{3+} ions with high selectivity and sensitivity.

Introduction

In the last decades, fluorescent composites have attracted increasing attention due to their extensive utility for: sensors,[1] photodynamic therapy,[2] solar cells,[3] gas storage and separation.[4] However, most fluorescent porous composites are fabricated from conventional monomers, which restrict generation of materials with novel properties.[5]

Cubic octasilsesquioxanes are ideal building blocks, often used to construct hybrid porous composites due to their 3-D structures, rigid skeletons, nano size (1–3 nm), high thermal stability and eight functional groups placed equally in Cartesian space.[6] As a prominent example, octavinylsilsesquioxane (OVS) provides access to new cage compounds *via* functionalization wherein the excited state exists as a spherical LUMO in the cage center leading to novel photophysical properties.[7] Very recently, several fluorescent hybrid porous materials based on OVS and conventional fluorophores have been reported.[8] Unfortunately, these materials suffer from short emission wavelengths, small Stokes shifts and poor emission intensities.[9] Thus, there is motivation to develop superior emissive systems especially using OVS as it provides the opportunity to place fluorophores in spherical arrays around the cage and introduce porosity.

Recently, fluorophores with near-infrared emission (NIR, $\lambda_{em} > 650$ nm) have received increasing attention due to their potential advantages in meeting challenges related to light scattering, auto-fluorescence from physiologically important materials, photo-bleaching, and optical absorption.[10] Most conventional NIR organic fluorophores that exhibit aggregation-caused quenching (ACQ) display intense fluorescence in dilute solutions but quenched emissions in aggregated forms or the solid state. This change in emission behavior is attributed to the formation of strong intermolecular π-π interactions and intramolecular rotations.[11]

Aggregation-induced emission (AIE) is the complete opposite of ACQ, and has recently emerged as an unique synthetic target to functionally useful new molecules and materials.[12] As might be anticipated, AIE fluorophores generally exhibit reduced emission in dilute solutions and enhanced emission in aggregated or solid states.[13] This feature is attributed to inhibition of intramolecular rotation, intermolecular dipole contacts and π-π interactions.[11,14] For example, the ACQ-active fluorophore, 2-[2.6-bis(-4-(diphenylamino)-stryryl-4H-pyranylidene]malono-nitrile (TPA-DCM) possesses a conjugated "D-π-A-π-D" configuration, dual intramolecular charge transfer (ICT) processes, and shows reduced NIR emission when aggregated.[15] To overcome these issues functional groups such as tetraphenylethene (TPE) can be introduced to transform ACQ to AIE.[16]

Facile "one-pot" methods are always preferred strategies for molecular engineering. For example, transforming ACQ to AIE active NIR fluorophores can involve simply introducing methyl groups to block preferred packing thereby transforming ACQ fluorophores to AIE fluorophores. In principle, this is much easier than conventional tailoring wherein one introduces an AIE functional fragment.[17] AIE active [2-(2,6-bis((E)-4-(di-p-tolylamino)styryl)-4H-pyran-4-ylidene]malononitrile (M-TPA-DCM) offering NIR emissive properties was synthesized *via* Knoevenagel reaction allowing a "one-pot" strategy. M-TPA-

[a] *Y. Yan, Dr. H. Liu*
Key Laboratory of Special Functional Aggregated Materials
Ministry of Education
School of Chemistry and Chemical Engineering, Shandong University
Jinan (P.R. China)
E-mail: liuhongzhi@sdu.edu.cn
[b] *Dr. R. M. Laine*
Macromolecular Science and Engineering
University of Michigan
Ann Arbor (USA)

Supporting information for this article is available on the WWW under https://doi.org/10.1002/cplu.201900568

DCM exhibits intensive emission in aggregated or solid-state due to the AIE effect and perhaps "σ-π" electron donating effects from methyl to TPA thereby promoting AIE and preferable emission of M-TPA-DCM. Coupling a conjugated "D-π-A-π-D" structure and dual ICT processes from two donors (M-TPA) to one acceptor (DCM), ensures NIR emission (680 nm). Methylation triggering conversion of ACQ to AIE emission provides a novel and useful strategy for preparing AIE active fluorophores perhaps enhancing the potential utility in many fields.

Ozin et al. reported some near infrared fluorescent porous composites by the thermal hydrosilylation of silicon nanocrystals (ncSi) with OVS.[18] Compared with silicon nanocrystals, organic fluorophores possesses good compatibility, facile preparation and tenability. However, there are no reports of organic fluorophore–silsesquioxane based NIR porous composites to the best of our knowledge. AIE-active fluorophore-based composites exhibit intense emissions at high loading contents, to date such materials are almost exclusively obtained by simply adding AIE-active monomers in an approach that still meets various challenges including damaging the original scaffold molecule or changing desired electronic interactions. Therefore, "one pot" *in situ* generation of AIE might offer a simple, valuable alternative especially as it converts the fluorophore emission mode from ACQ to AIE coincident with materials synthesis.

The well-recognized transformation of the ACQ emission mode of TPA-DCM to AIE-active emission in M-TPA-DCM by simple methylation prompted us to explore Friedel-Crafts modification to transform ACQ to AIE while also producing several hybrid porous materials through direct formation of alkyl bridge between TPA-DCM and OVS, *i.e.* TPAIEs. Moreover, these TPAIEs exhibit tunable porosities (S_{BET} from 160 to 720 $m^2 g^{-1}$, pore volumes from 0.13–0.55 $cm^3 g^{-1}$), NIR emission (670 nm) and excellent thermal stability.

As a toxic species, Ru^{3+} can be found widely in various industrial fields,[19] and remains a challenge for real time monitoring. Compared with conventional homogeneous detection methods, heterogeneous monitoring may avoid over loading/overdosing testing systems. Interestingly, the electron-rich properties coupled with porosity endows TPAIEs with advantages for detecting trace quantities of Ru^{3+} at 10^{-8} M, rapid response times (within 20 s), high selectivity and sensitivity. In the following sections we detail our approach to the molecular strategy using methylation tailoring of ACQ organic fluorophore to obtain AIE and preferable NIR organic fluorophore coincident with the opportunity to fabricate emission enhanced NIR functional porous composites.

Results and Discussion

AIE Feature of M-TPA-DCM

As a typical ACQ active NIR fluorophore, the emission and UV-vis absorbance spectra of TPA-DCM have been reported previously.[15] However, to our knowledge, the fluorescence properties of M-TPA-DCM remain unexplored. Methyl modified M-TPA-DCM exhibits quite bright red emission in the solid state (Figure 1(a)). The normalized absorption and emission spectra of M-TPA-DCM in dry DMF are recorded in Figure 1(b). The absorbance and emission bands at 490 and 680 nm (NIR region), respectively, ensure a larger Stokes shift (190 nm) than many other organic fluorophores. Compared with TPA-DCM, a slight (5 nm) red shift of absorbance and emission of M-TPA-DCM likely arises from the added methyl, and is consistent with the slight change in band gap from the theoretical calculation showing that M-TPA-DCM $\Delta E = 2.79$ eV is slightly lower than TPA-DCM $\Delta E = 2.84$ eV (Figure S1).

M-TPA-DCM exhibits solvent effects, *i.e.* red-shifts and reduced emission signal vs. increasing solvent polarity, which is attributed to a twisted intramolecular charge transfer (TICT) state (Figure S2).[20] The AIE properties of M-TPA-DCM in 0 to 90% (f_w) DMF–water mixtures are presented in Figure 1(c) showing that emission decreases mildly with increasing water fraction from 0 to 30%, due to the internal TICT effect of the dual D-A structure caused by the increased solvent polarity and reduction of solubility. With further increases in f_w, the fluorescent emission signal increases significantly ($30\% < f_w < 80\%$), and reaches a maximum of 15 fold enhancement at $f_w = 80\%$ (Figure 1(d)). The added methyl group likely reduces intramolecular rotation and intermolecular π-π stacking in the aggregated state, promoting active AIE feature. A reduced fluorescence emission signal is expressed for further increments in f_w (>90%) since significant M-TPA-DCM aggregation enhances twisted intramolecular charge transfer (TICT) effect.[21] These results suggest that AIE active M-TPA-DCM offers superior NIR emission (680 nm).

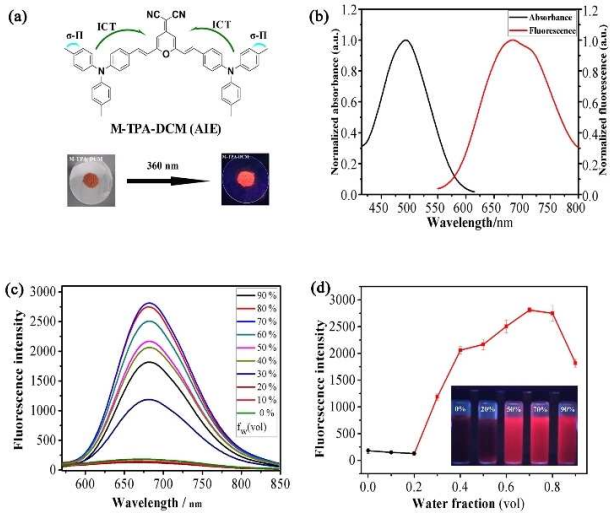

Figure 1. (a) The molecular structure of M-TPA-DCM. **(b)** Normalized UV-Vis absorption and emission spectra of M-TPA-DCM in DMF solution. **(c)** Fluorescence emission spectra of M-TPA-DCM in water/DMF mixtures with various water fractions f_w. **(d)** Plot of maximum intensity of M-TPA-DCM versus water fraction in water/DMF mixed solvent. ([M-TPA-DCM] = 10^{-5} M, λ_{ex} = 485 nm, speed: 2400 nm/min, slit: 5/5.)

Crystal Structure of TPA-DCM and M-TPA-DCM

To further explore the source of AIE, the structure, interaction and packing behavior of crystalline TPA-DCM and M-TPA-DCM were studied. The phenyl rings on TPA fragments show various rotational angles, revealing a twisted "D-π-A-π-D" geometry (Figure 2(a)). TPA-DCM falls in the $P2_1/n$ space group with $Z=4$ (Figure 2(b) and Table S1 in the Supporting Information). TPA-DCM packs parallelly in a rhombic column along the "b" direction, while TPA fragments are arranged alternately at the periphery of the column and DCM packing occurs along the central axis of the column (Figure 2(c)).

The close "face to face" stacking ensures effective "π-π" interaction [Figure 2(d)] inducing quenched and red-shifted emission in aggregated state.[22] The points of closest approach between "C≡N" and "H" are ≈2.516 Å and 2.730 Å, arising from contacted bonding in aggregated state (Figure 2(e)). The dipole-dipole interactions lead to red-shifted emissions in solid state.[23] Reduced short contacts with TPA enhance intramolecular rotation of phenyls weakening fluorescence from TPA-DCM in aggregated state.

M-TPA-DCM exhibits the same $P2_1/n$ space group with $Z=4$ (Figure 3(b) and Table S2). M-TPA-DCM possesses a more relaxed "V-shaped" conformation, relatively uniform rotation angles and better symmetry (Figure 3(a)), perhaps arising from reduced ICT effects from "σ-π" electron donation from methyl to TPA. M-TPA-DCM exhibits rhombic packing along the "b" direction. M-TPA is arranged alternately at the periphery (Figure 3(c)). The centroid-centroid distance of "DCM-DCM" (4.2 Å) is longer than between contiguous DCM planes (3.2 Å), which eliminates face to face π-π stacking interactions in the crystal (Figure 3(d)).[24] In aggregated M-TPA-DCM, methyl enhances the interaction between M-TPA and DCM, relieving the dipole-dipole (DCM-DCM) interactions effectively [Figure 3(e)]. The multiple intermolecular interactions in M-TPA lock the molecular conformation and constrain rotation of phenyls effectively, which causes enhanced and unshifted emission in aggregated state.[25]

Fabrication and Characterization of NIR Porous Composites

TPAIEs were fabricated from OVS and TPA-DCM based on Friedel-Crafts chemistry. In the FTIR, the values at 1110, 1617 and 2210 cm^{-1} are ascribed to Si–O–Si, C=C and C≡N vibration and, respectively. The bands at 1110 and 2210 cm^{-1} coexist in the resulting composites (Figure S3), arising from the Friedel-Crafts transformation between OVS and TPA-DCM. The band at 1617 cm^{-1} likely arises from unreacted vinyl ($\nu_{C=C}$). This band grows gradually with increasing OVS dosage. Solid state ^{29}Si CP/MAS NMR spectrum was recorded in support of this successful Friedel-Crafts reaction. The ^{29}Si MAS NMR of TPAIE-2 shows three major peaks at 81.6, 70.3 and 66.8 ppm. The signal at −81.6 ppm is attributed to Si with unreacted vinyl groups. The signals at −66.8 and −70.3 ppm are assigned to silicon atoms of T_3 ($Tn:Si(OSi)n(OH)_{3-n}$) units of Si–CH_2–CH_2–TPA-DCM or Si–CH_2(CH_3)-TPA-DCM after Friedel-Crafts reaction (Figure S4).

TGA studies show that TPAIEs offer $Td_{5\%}$ at >400 °C, higher than 360 °C of TPA-DCM likely because of the introduction of the silica core (Figure S5).[26] PXRD presents diagnostic peaks for OVS (8.9°, 12.7°, 19.6°, 28.4°, 29.3°, 37.2° and 40.1°) and TPA-DCM (9.0°, 12.9°, 18.5° and 26.2°) disappear in the composites except for 2θ≈22° (quartz substrate) (Figure S6). HR-TEM of TPAIE-2 suggests its amorphous character, consistent with the PXRD data, and disordered porous structure (Figure S7(a) and

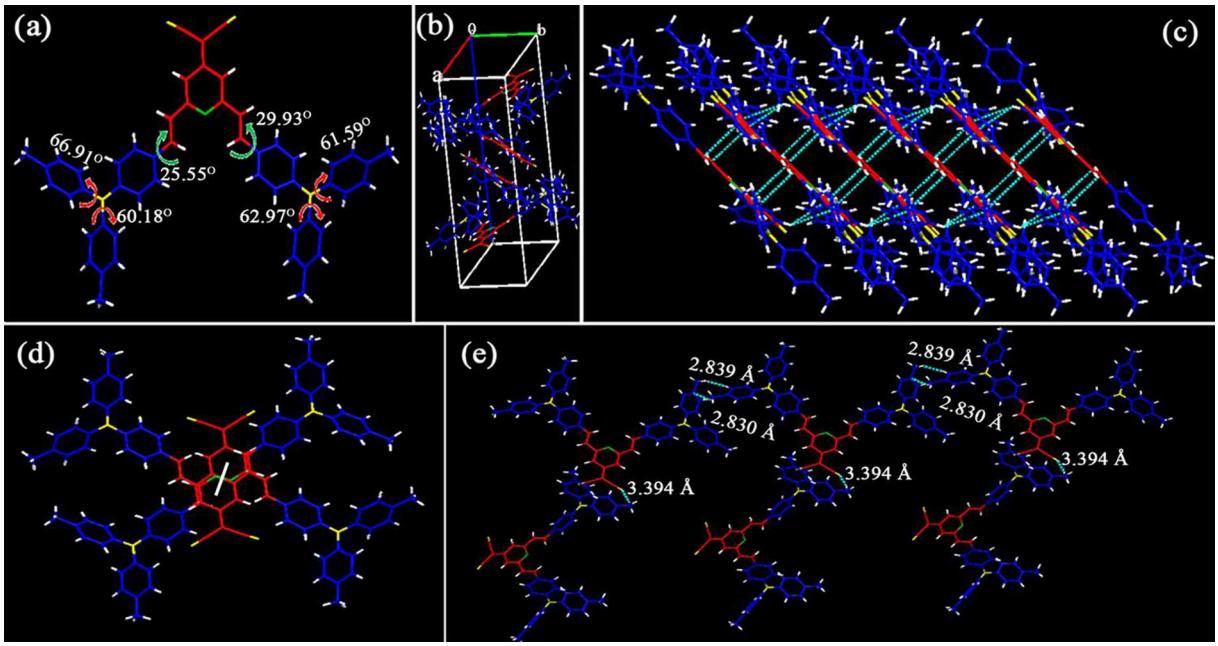

Figure 2. Single-crystal structure of TPA-DCM: **(a)** Molecular structure of TPA-DCM in crystal. **(b)** Crystal cell for TPA-DCM in b direction. (c) Molecular packing manner of TPA-DCM in c direction. **(d)** Intermolecular interactions of TPA-DCM, and **(e)**.

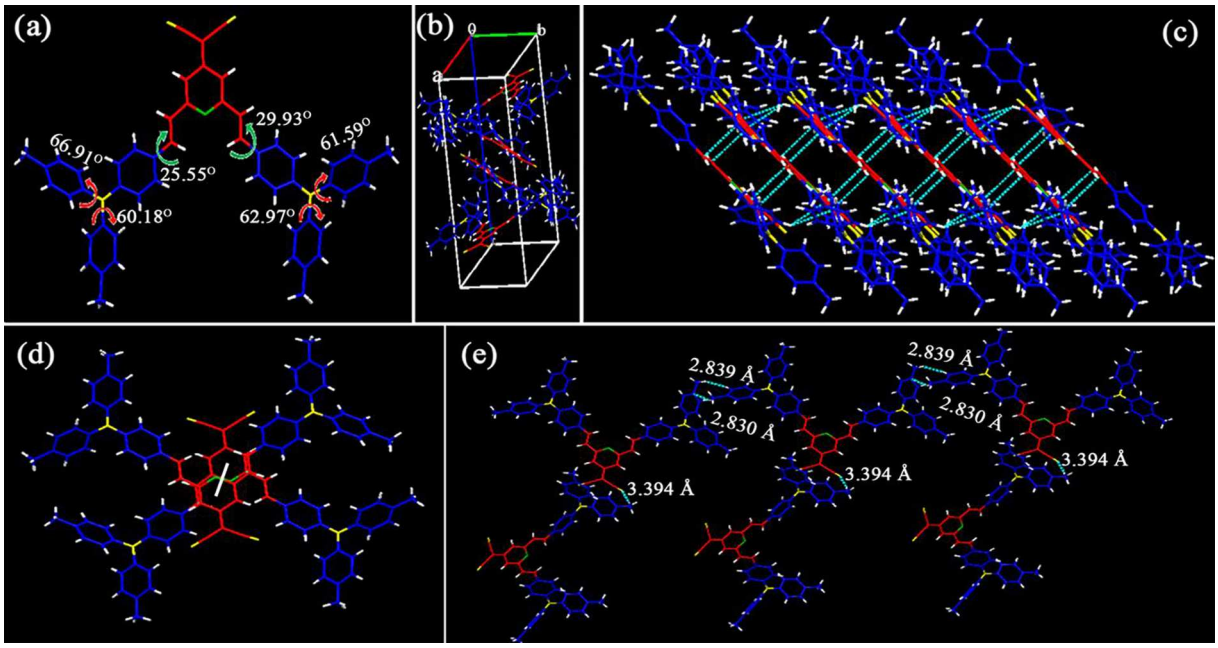

Figure 3. Single-crystal structure of M-TPA-DCM: **(a)** Molecular structure of M-TPA-DCM in crystal. **(b)** Crystal cell for M-TPA-DCM in b direction. **(c)** Molecular packing manner of M-TPA-DCM in c direction. **(d)** Intermolecular interactions of M-TPA-DCM and **(e)**.

(b)). FE-SEM shows that TPAIE-2 exists as agglomerated granules (Figure S8(c) and (d)).

Porosity

N_2 BET studies at 77 K are presented as Figure 4(a). Both TPAIE-1 and TPAIE-2 offer parallel adsorption and desorption profiles with sharp uptakes at low relative pressure and high relative pressure with a clear hysteresis. In contrast, TPAIE-3 exhibits rapid intake at low relative pressures and slowly increasing uptake at high relative pressure with a good defined hysteresis loop. Consequently, micro- and mesoporosity coexist.[27] BET measurements provide explicit surface areas (S_{BET}) of 160, 720 and 640 $m^2 g^{-1}$ respectively. Microporous S_{BET} were 60, 320 and 210 $m^2 g^{-1}$ by t-plot patterns (Table S3). S_{BET} and microporous S_{BET} of TPAIEs increase initially, and decrease gradually with further increasing OVS molar ratio. The maximum S_{BET} and microporous S_{BET} were calculated as 720 and 320 $m^2 g^{-1}$ when the molar ratio of OVS/TPA-DCM was 1.5:1, *i.e.* TPAIE-2. Considering its big volume and rigid molecular structure, OVS becomes more and more difficult to react with TPA-DCM with increasing OVS dosage due to steric hindrance.[28] Increasing OVS content provides more reactive sites and enhances cross-link densities while coincidentally increasing unreacted vinyl contents and reducing S_{BET}.[29] Hence, tunable porosities are afforded.

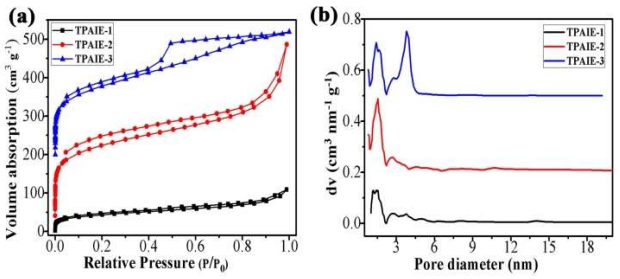

Figure 4. (a) Nitrogen adsorption-desorption isotherms of TPAIEs at 77 K. **(b)** The NL-DFT pore size distribution of TPAIEs.

Pore size distribution (PSD) profiles for TPAIE-1 and TPAIE-2 are centered at 1.41, 1.54 nm respectively, while TPAIE-3 possesses a bimodal pore size distribution curve with peaks at 1.44 and 3.79 nm. The result is ascribed to higher cross-linking with increasing OVS content, which favors mesopores.[30] The total pore volumes (V_{total}) are 0.13, 0.55 and 0.45 $cm^3 g^{-1}$, respectively; meanwhile, the microporous volumes (V_{micro}) are 0.03, 0.16 and 0.09 $cm^3 g^{-1}$, respectively. Although the main PSD peak for TPAIE-1 and TPAIE-2 indicates they are micropores, continuous multistage pore size distributions provide higher mesoporous volumes and lower V_{micro}/V_{total} ratios.

Different pore size distribution profiles for TPAIEs suggest mesoporous composites since low ratio of V_{micro}/V_{total} (0.23, 0.29 and 0.20) (Table S3) are formed.

Fluorescence Investigation

The fluorescent emissions of TPA-DCM, M-TPA-DCM and TPAIEs in solid state are presented in (Figure 5(a)). TPA-DCM exhibits reduced emission signal and 30 nm red-shifted emission windows (705 nm) in solid state arising from ACQ. In contrast, M-TPA-DCM exhibits AIE-active and unshifted emission (680 nm) in the solid state due to the absence of π-π and

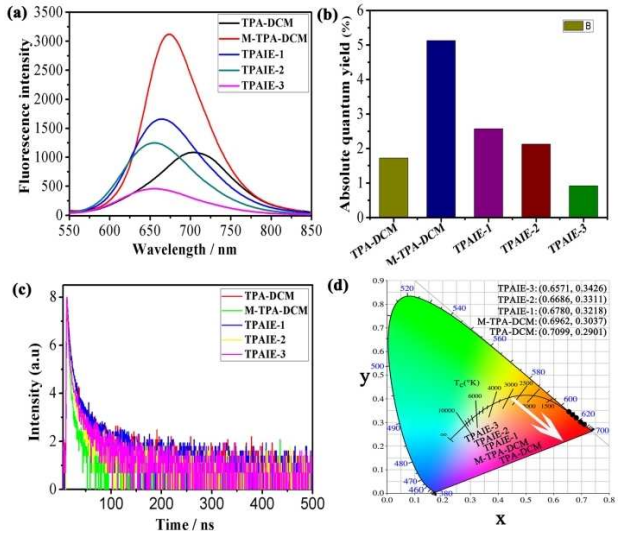

Figure 5. **(a)** The emission spectra of TPA-DCM, M-TPA-DCM and TPAIEs in solid state. **(b)** Absolute fluorescent quantum yield of TPA-DCM, M-TPA-DCM and TPAIEs in solid state. **(c)** The time-dependent fluorescence of TPA-DCM, M-TPA-DCM and TPAIEs. **(d)** CIE chromaticity diagram for TPA-DCM, M-TPA-DCM and TPAIEs.

dipole-dipole interactions. The solid fluorescence of TPA-DCM and M-TPA-DCM agrees with the single crystal analysis.

For hybrid porous materials, the "C" atom at the counterpoint of "N" in TPA-DCM likely reacts with an OVS vinyl due to the higher electron density and weaker steric hindrance based on the mechanism of Friedel-Crafts reaction (Scheme 1). For example, the formation of TPAIE-1 (the molar ratio of OVS and TPA-DCM is 1:2) occurs through introduction of alkyl bridges between TPA-DCM and OVS switching emission mode from ACQ to AIE.

Simplification and geometry optimization of TPAIE-1 were conducted in theoretical simulation indicating the energy band gap $\Delta E = 2.81$ eV was close to M-TPA-DCM $\Delta E = 2.79$ eV (Figure S1 in the Supporting Information). Therefore, *in situ* generated AIE is observed in TPAIE-1 as expected. In Figure 5(a), TPAIE-1 exhibited stronger emission and 1.7 folds enhancement

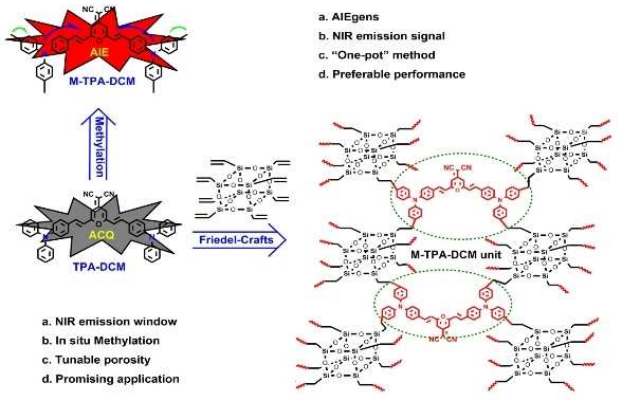

Scheme 1. The fabrication of emission-enhanced NIR functional composites (TPAIES).

over TPA-DCM in solid state due to AIE effect. In contrast, blue-shifted emission of TPAIE-1 arises since π-π interactions interdicted.

Generally, the reaction of OVS with ACQ-active TPA-DCM will eliminate or reduce π-π stacking interactions and intramolecular rotation of TPA-DCM, inducing gradually enhanced emission with increasing OVS dosage. Interestingly, TPAIEs showed gradually reduced emission signals from TPAIE-1 to TPAIE-3 and even 5 folds decreased for TPAIE-3 [Figure 5(a)], the absolutely opposite of the hybrid fluorescence of the porous composites from Friedel-Crafts of OVS with pristine triphenylamine.[31] The opposite changes of emission implied there were in situ generation of the AIE-active moiety in TPAIEs. The gradually reduced emission signals in TPAIEs are caused by preventing aggregation of the AIE-active M-TPA-DCM moiety with increasing OVS molar ratio. The absolute fluorescence quantum yields (Φ_f) of TPA-DCM, M-TPA-DCM, TPAIE-1, TPAIE-2 and TPAIE-3 in the solid state were measured as 1.3%, 5.1%, 3.2%, 2.5% and 1.1%, respectively, which agree with the variation in emission spectra [Figure 5(b)]. The variation not only reveals their excellent fluorescent properties but also further indicates *in situ* generation of an AIE moiety. In addition, a slight blue shifted emission window was observed on going from TPAIE-1 to TPAIE-3 due to non-dipole and dipole interactions from the unreacted vinyl and DCM in the porous network.[32]

The time-resolved fluorescence measurements for TPAIEs in solid state displayed lifetimes ranging from 18.7 to 24.2 ns, which indicates that fluorescent lives can be tuned facilely by changing the OVS/TPA-DCM molar ratios [Figure 5(c)]. Besides, these results also show that M-TPA-DCM, TPA-DCM and TPAIEs possess stable emission signal output in the solid state. The emission chromaticity was clearly observed from their emission spectra by CIE-1931 RGB coordinates, and showed deeply red color including TPA-DCM (0.7099, 0.2901), M-TPA-DCM (0.6962, 0.3037), TPAIE-1 (0.6780, 0.3218), TPAIE-2 (0.6686, 0.3311), TPAIE-3 (0.6571, 0.3426) [Figure 5(d)]. The variation of chromaticity of red was consistent with the emission window shift and emission intensity, and revealing their highly pure red and NIR emission feature. Hence, a family of organic fluorophore–silsesquioxane based hybrid porous materials with NIR emission window, tunable emission signal and steady emission lifetime were fabricated depended on in situ AIE strategy.

Selectivity for Ru^{3+} Ions

Considering its high surface area (S_{BET}), TPAIE-2 was selected to explore the application in metal ions detection. As a crucial criterion for sensor, the selectivity of TPAIE-2 for metal ions was explored and showed special selectivity for Ru^{3+} (Figure 6(a) and (b)). Although various metal ions including Cu^{2+}, Fe^{3+}, Ni^{2+}, Co^{2+}, Zn^{2+}, Mg^{2+}, Cd^{2+}, Al^{3+}, Ag^{+}, Hg^{2+}, Mn^{2+}, Pb^{2+}, F^{-}, Cl^{-}, Br^{-}, I^{-}, HCO_3^{-}, S^{2-}, CO_3^{2-}, HPO_4^{2-}, SO_4^{2-}, NO_3^{-} and SO_3^{2-} (1.0×10^{-3} mol L^{-1}, V_{DMF}:V_{water} = 5:5) were conducted, the emission signal did not clearly decrease compared with the blank group.

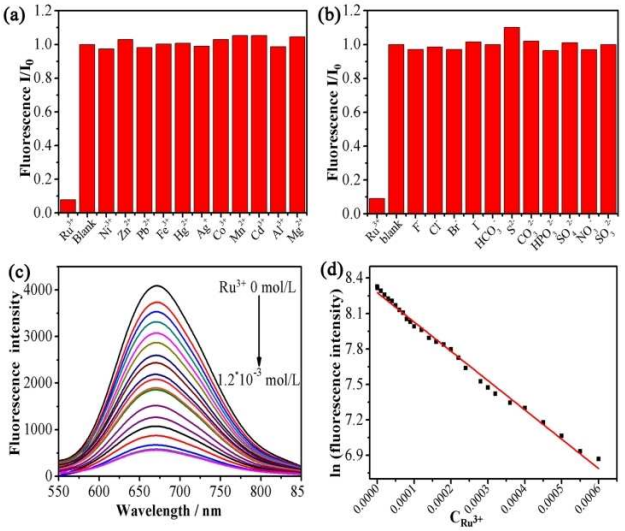

Figure 6. **(a)** The selectivity of TPAIE-2 for Ru^{3+} in the presence of various metal ions. **(b)** Selectivity of TPAIE-2 for Ru^{3+} in the presence of various anions. **(c)** Fluorescence intensity variation of TPAIE-2 for the increment of Ru^{3+}. **(d)** The linearity of Ln (I) of TPAIE-2 to Ru^{3+}.

However, the fluorescent emission signal realized 8 folds decrements and even quenched completely after the same amount of Ru^{3+} was added, which revealed that TPAIE-2 exhibited higher selectivity for Ru^{3+} than many other composites reported.[8,31] The result can be attributed to the electron transfer process from electron-rich composites to Ru^{3+}*via* electron transfer platform.[33] To further confirm this mechanism, we measured the UV-vis absorbance spectrum of Ru^{3+} and fluorescence emission spectrum of TPAIE-2. It was observed that two curves did not overlap (Figure S8). Therefore, the quenched emission couldn't be ascribed to energy transfer from TPAIE-2 to Ru^{3+}. Meanwhile, the UV-vis absorbance spectra of Ru^{3+} and TPAIE-2 remain some distance and do not overlap, further revealing that the quenched emission could not be attributed to inner-filter effects yet, *i.e.* the reduced excitation energy was caused by absorbing Ru^{3+} (Figure S8). Besides, high surface areas, hierarchical pore structures and electron-rich features allow TPAIE-2 to specifically respond to Ru^{3+}. For example, TPE decorated HOF derived from silesquioxane cages exhibits specific sensitivity to Cu^{2+},[34] whereas, TPE-silesquioxane based porous composites respond to Fe^{3+}, Ru^{3+} and Cu^{2+}, effectively.[25]

With increasing Ru^{3+}, the fluorescence emission signal decreases gradually and even 8-fold decrements were observed at quenching equilibrium when $C_{Ru}{}^{3+}$ achieved 10^{-3} mol L^{-1} (Figure 6(c)). Meanwhile, The linear function between Ln (I) and $C_{Ru}{}^{3+}$ ranging from 0 mol L^{-1} to 6×10^{-4} mol L^{-1} was plotted ($K=-2479$, $\sigma=0.9930$) to reveal the potential of TPAIE-2 for quantitatively monitoring Ru^{3+}, especially at low $C_{Ru}{}^{3+}$ [Figure 6(d)]. Therefore, the equation between [Ru^{3+}] and fluorescent intensity was plotted as $y=8.28-2479x$. To explore the sensitivity of TPAIE-2 to Ru^{3+}, the quenched degree was estimated by quenching constant (K_{SV}) from the equation $I_0/I=1+K_{sv}[Ru^{3+}]$. K_{sv} was calculated to 5300, which revealed the high sensitivity of TPAIE-2 to Ru^{3+}. Hence, TPAIE-2 possesses various advantages for t detecting Ru^{3+} including a low detection limit, high sensitivity and selectivity, which strongly suggests its utility as a significant candidate for detecting Ru^{3+}. Note that human tissue is nearly transparent to NIR at >650 nm.[35] Therefore, this hybrid NIR porous material may provide potential for sensing metal ions *in vivo,* bioimaging and perhaps photodynamic therapy.[36]

Conclusion

A novel method was developed to modify ACQ active organic fluorophore by in situ methylation to realize AIE properties and selective fluorescence. Methylation of TPA-DCM resulted in an AIE active and D-π-A-π-D conjugated M-TPA-DCM. In addition, a family of organic fluorophore–silsesquioxane based NIR hybrid porous composites with AIE-active units was prepared by Friedel-Crafts reaction of TPA-DCM with OVS for the first time. Moreover, tunable porosity and emission signal was realized by changing the molar ratio of monomers. Consequently, the resulting composites exhibited NIR emission, high thermal/light stability, multistage porous structure and high surface area. High surface area, hierarchical pore structure and electron-rich feature of the composite ensure the monitoring of Ru^{3+} with low detect limit, high selectivity and sensitivity. Importantly, the in situ AIE strategy innovated a new way to develop advanced functional molecules or composites.

Experimental Section

Synthesis of TPA-DCM

2-(2.6-bis((E)-4-(diphenylamino)-stryryl-4H-pyran-ylidene) malononitrile (TPA-DCM) was synthesized according to the reported experimental procedures (Scheme S1).[13]

Synthesis of M-TPA-DCM

2-(2,6-bis((E)-4-(di-p-tolylamino)styryl)-4H-pyran-4-ylidene) malononitrile (M-TPA-DCM) was synthesized according to the Scheme S1 based on Knoevenagel condensation. 4-(di-p-tolylamino)benzaldehyde (M-TPA, 2.4 mmol, 0.72 g) and 2-(2,6-dimethyl-4H-pyran-4-ylidene)-malononitrile (DCM, 1.0 mmol, 0.17 g) were dissolved into dried CH_3CN (20.0 mL). The mixtures were heated to refluxing and maintain 24 h under the catalysis of piperidine. After distillation under reduced pressure, the solvent was removed. Then, the products were purified by column chromatography on silica gel and ethyl acetate/petroleum ether (V/V 1/15) as the developing solvent. M-TPA-DCM was obtained as red brown powder with 72% yield. This structure was confirmed by following methods: Single crystal diffraction (Figure 2 and Figure 3); ^{1}H NMR (500 MHz, DMSO-d_6), δ (ppm): 2.341 (s, 12H), 6.559 (d, 2H, J = 16.0 Hz), 6.606 (s, 2H), 6.968 (d, 4H, J = 9.0 Hz), 7.045 (dd, 8H, J = 1.5 and 6.5 Hz), 7.116 (d, 8H, J = 8.0 Hz), 7.362 (d, 4H, J = 8.5 Hz), 7.430 (d, 2H, J = 16.0 Hz) (Figure S9); ^{13}C NMR (125 MHz, DMSO-d_6), δ (ppm): 20.918, 106.125, 115.159, 115.845, 120.324, 125.741, 126.584, 128.964, 130.191, 134.161 137.580, 144.127, 150.397, 155.953, 158.907 (Figure S10). HR-MS m/z: Calcd for $C_{52}H_{42}N_4O$, $[M+H]^+=739.3431$, found: 739.3425, 739.3473 (Figure S11).

[CCDC 1908474 contains the supplementary crystallographic data of M-TPA-DCM for this paper. These data can be obtained free of charge from The Cambridge Crystallographic Data Centre via www.ccdc.cam.ac.uk/data_request/cif.]

[CCDC 1908477 contains the supplementary crystallographic data of TPA-DCM for this paper. These data can be obtained free of charge from The Cambridge Crystallographic Data Centre via www.ccdc.cam.ac.uk/data_request/cif.]

Fabrication of NIR Porous Composites (TPAIEs)

TPAIEs were fabricated from OVS and TPA-DCM based on Friedel-Crafts reaction according to various ratios of monomers (Table S1). Typically, TPAIE-1 was prepared as following: OVS (0.25 mmol, 0.16 g), anhydrous aluminium chloride (1 mmol, 0.24 g) and monomer 1 (0.5 mmol, 0.34 g) were added into dried three necked vessel and dissolved into dried 1.2-dichloroethane (25.00 mL). After the stirring in room temperature for 0.5 h, the mixtures were heated to refluxing for 24 h. After cooling to room temperature, the resulting mixtures were filtered under reduced pressure and washed with anhydrous ethanol (50 mL×4), tetrahydrofuran (50 mL×4), chloroform (50 mL×4), acetone (50 mL×4) respectively. Then, Soxhlet extractor was employed to further purify with methanol and dichloromethane respectively for 24 h. Finally, the resulting product is dried under vacuum for 24 h at 100 °C.

Acknowledgements

This research was supported by the National Natural Science Foundation of China (NSFC) (No. 21574075, 21975144), Key Research, Development Program of Shandong province (No. 2018GGX102034), Ministry of Science and Technology of the People's Republic of China (G20190015037) and Seed Fund Program for the International Research Cooperation of Shandong University. RML thanks the SJTU/UM joint institute for sabbatical support during the writing of this manuscript.

Conflict of Interest

The authors declare no conflict of interest.

Keywords: aggregation-enhanced emission · fluorophores · near-infrared emission · porous materials · silsesquioxanes

[1] P. Wu, J. Wang, C. He, X. Zhang, Y. Wang, T. Liu, C. Duan, *Adv. Funct. Mater.* **2012**, *22*, 1698–1703.
[2] C. Mauriello Jimenez, D. Aggad, J. G. Croissant, K. Tresfield, D. Laurencin, D. Berthomieu, N. Cubedo, M. Rossel, S. Alsaiari, D. H. Anjum, R. Sougrat, M. A. Roldan-Gutierrez, S. Richeter, E. Oliviero, L. Raehm, C. Charnay, X. Cattoën, S. Clément, M. W. C. Man, M. Maynadier, V. Chaleix, V. Sol, M. Garcia, M. Gary-Bobo, N. M. Khashab, N. Bettache, J.-O. Durand, *Adv. Funct. Mater.* **2018**, *28*, 1800235.
[3] Y. X. Ma, Z. J. Li, L. Wei, S. Y. Ding, Y. B. Zhang, W. Wang, *J. Am. Chem. Soc.* **2017**, *139*, 4995–4998.
[4] H. Wang, B. Li, H. Wu, T. L. Hu, Z. Yao, W. Zhou, S. Xiang, B. Chen, *J. Am. Chem. Soc.* **2015**, *137*, 9963–9970.
[5] R. Shen, H. Liu, *RSC Adv.* **2016**, *6*, 37731–37739.
[6] a) X. Chen, L. F. Dumée, *Adv. Eng. Mater.* **2019**, *21*, 1800667; b) K. Wu, M. Huang, K. Yue, C. Liu, Z. Lin, H. Liu, W. Zhang, C. H. Hsu, A. C. Shi, W. B. Zhang, S. Z. D. Cheng, *Macromolecules* **2014**, *47*, 4622–4633.
[7] a) J. C. Furgal, J. H. Jung, T. Goodson, R. M. Laine, *J. Am. Chem. Soc.* **2013**, *135*, 12259–12269; b) M. Z. Asuncion, R. M. Laine, *J. Am. Chem. Soc.* **2010**, *132*, 3723–3736.
[8] Y. Du, H. Liu, *ChemistrySelect* **2018**, *3*, 1667–1673.
[9] R. Sun, X. Huo, H. Lu, S. Feng, D. Wang, H. Liu, *Sens. Actuators B* **2018**, *265*, 476–487.
[10] a) J. Qi, C. Sun, D. Li, H. Zhang, W. Yu, A. Zebibula, J. W. Y. Lam, W. Xi, L. Zhu, F. Cai, P. Wei, C. Zhu, R. T. K. Kwok, L. L. Streich, R. Prevedel, J. Qian, B. Z. Tang, *ACS Nano* **2018**, *12*, 7936–7945. b) Y. Yuan, C. J. Zhang, M. Gao, R. Zhang, B. Z. Tang, B. Liu, *Angew. Chem. Int. Ed.* **2015**, *54*, 1780–1786; *Angew. Chem.* **2015**, *127*, 1800–1806.
[11] a) J. Wang, X. Gu, P. Zhang, X. Huang, X. Zheng, M. Chen, H. Feng, R. T. K. Kwok, J. W. Y. Lam, B. Z. Tang, *J. Am. Chem. Soc.* **2017**, *139*, 16974–16979;b) W. Fu, C. Yan, Z. Guo, J. Zhang, H. Zhang, H. Tian, W. H. Zhu, *J. Am. Chem. Soc.* **2019**, *141*, 3171–3177.
[12] a) D. Wang, H. Su, R. T. K. Kwok, X. Hu, H. Zou, Q. Luo, M. M. S. Lee, W. Xu, J. W. Y. Lam, B. Z. Tang, *Chem. Sci.* **2018**, *9*, 3685–3693; b) Y. Jiang, N. Hadjichristidis, *Macromolecules* **2019**, *52*, 1955–1964.
[13] a) H. Q. Peng, B. Liu, P. Wei, P. Zhang, H. Zhang, J. Zhang, K. Li, Y. Li, Y. Cheng, J. W. Y. Lam, W. Zhang, C. S. Lee, B. Z. Tang, *ACS Nano* **2019**, *13*, 839–846; b) J. S. Ni, P. Zhang, T. Jiang, Y. Chen, H. Su, D. Wang, Z. Q. Yu, R. T. K. Kwok, Z. Zhao, J. W. Y. Lam, B. Z. Tang, *Adv. Mater.* **2018**, *30*, 1805220.
[14] a) L. Pan, H. Wu, J. Liu, K. Xue, W. Luo, P. Chen, Z. Wang, A. Qin, B. Z. Tang, *Adv. Opt. Mater.* **2019**, *7*, 1801673; b) X. Ni, X. Zhang, X. Duan, H. L. Zheng, X. S. Xue, D. Ding, *Nano Lett.* **2019**, *19*, 318.
[15] W. Qin, D. Ding, J. Liu, W. Z. Yuan, Y. Hu, B. Liu, B. Z. Tang, *Adv. Funct. Mater.* **2012**, *22*, 771–779.
[16] a) Z. Sheng, B. Guo, D. Hu, S. Xu, W. Wu, W. H. Liew, K. Yao, J. Jiang, C. Liu, H. Zheng, B. Liu, *Adv. Mater.* **2018**, *30*, 1800766; b) J. Lin, X. Zeng, Y. Xiao, L. Tang, J. Nong, Y. Liu, H. Zhou, B. Ding, F. Xu, H. Tong, Z. Deng, X. Hong, *Chem. Sci.* **2019**, *10*, 1219–1226.
[17] X. Ni, X. Zhang, X. Duan, H. L. Zheng, X. S. Xue, D. Ding, *Nano Lett.* **2019**, *19*, 318–330.
[18] D. Chen, W. Sun, C. Qian, L. M. Reyes, A. P. Y. Wong, Y. Dong, J. Jia, K. K. Chen, G. A. Ozin, *Adv. Funct. Mater.* **2016**, *26*, 5102–5110.
[19] a) M. Venkatesan, K. I. Sathiyanarayanan, *Sens. Actuators B* **2018**, *267*, 373–380; b) L. Xu, T. Zhou, M. Liao, R. Hu, B. Z. Tang, *ACS Macro Lett.* **2019**, *8*, 101–106.
[20] a) D. Wang, H. Su, R. T. K. Kwok, G. Shan, A. C. S. Leung, M. M. S. Lee, H. H. Y. Sung, I. D. Williams, J. W. Y. Lam, B. Z. Tang, *Adv. Funct. Mater.* **2017**, *27*, 1704039; b) W. W. H. Lee, Z. Zhao, Y. Cai, Z. Xu, Y. Yu, Y. Xiong, R. T. K. Kwok, Y. Chen, N. L. C. Leung, D. Ma, J. W. Y. Lam, A. Qin, B. Z. Tang, *Chem. Sci.* **2018**, *9*, 6118–6125.
[21] a) A. Shao, Y. Xie, S. Zhu, Z. Guo, S. Zhu, J. Guo, P. Shi, T. D. James, H. Tian, W. H. Zhu, *Angew. Chem. Int. Ed.* **2015**, *54*, 7275–7280; *Angew. Chem.* **2015**, *127*, 7383–7388; b) X. Gu, X. Zhang, H. Ma, S. Jia, P. Zhang, Y. Zhao, Q. Liu, J. Wang, X. Zheng, J. W. Y. Lam, D. Ding, B. Z. Tang, *Adv. Mater.* **2018**, *30*, 1801065.
[22] C. Li, R. Duan, B. Liang, G. Han, S. Wang, K. Ye, Y. Liu, Y. Yi, Y. Wang, *Angew. Chem. Int. Ed.* **2017**, *56*, 11525–11529; *Angew. Chem.* **2017**, *129*, 11683–11687.
[23] S. M. Fateminia, Z. Wang, C. C. Goh, P. N. Manghnani, W. Wu, D. Mao, L. G. Ng, Z. Zhao, B. Z. Tang, B. Liu, *Adv. Mater.* **2017**, *29*, 1604100.
[24] J. Yang, X. Zhen, B. Wang, X. Gao, Z. Ren, J. Wang, Y. Xie, J. Li, Q. Peng, K. Pu, Z. Li, *Nat. Commun.* **2018**, *9*, 840.
[25] Z. Zheng, T. Zhang, H. Liu, Y. Chen, R. T. K. Kwok, C. Ma, P. Zhang, H. H. Y. Sung, I. D. Williams, J. W. Y. Lam, K. S. Wong, B. Z. Tang, *ACS Nano* **2018**, *12*, 8145–8159.
[26] P. Scholder, M. Hafner, A. W. Hassel, I. Nischang, *Eur. J. Inorg. Chem.* **2016**, *7*, 951–955.
[27] a) M. Ge, H. Liu, *J. Mater. Chem. A* **2016**, *4*, 16714–16722. b) R. Sun, S. Feng, D. Wang, H. Liu, *Chem. Mater.* **2018**, *30*, 6370–6376.
[28] a) F. Alves, P. Scholder, I. Nischang, *ACS Appl. Mater. Interfaces* **2013**, *5*, 2517; b) I. Nischang, O. Bruggemann, I. Teasdale, *Angew. Chem. Int. Ed.* **2011**, *50*, 4592.
[29] a) Z. Gou, Y. Zuo, M. Tian, W. Lin, *ACS Appl. Mater. Interfaces* **2018**, *10*, 28979–28991; b) S. Wang, L. Tan, C. Zhang, I. Hussain, B. Tan, *J. Mater. Chem. A* **2015**, *3*, 6542–6548.
[30] a) P. Scholder, I. Nischang, *Catal. Sci. Technol.* **2015**, *5*, 3917; b) H. Liu, H. Liu, *J. Mater. Chem. A* **2017**, *5*, 9156; c) F. Alves, I. Nischang, *Chem. Eur. J.* **2013**, *19*, 17310.

[31] R. Shen, Y. Liu, W. Yang, Y. Hou, X. Zhao, H. Liu, *Chem. Eur. J.* **2017**, *23*, 13465–13473.
[32] J. H. Jung, J. C. Furgal, S. Clark, M. Schwartz, K. Chou, R. M. Laine, *Macromolecules* **2013**, *46*, 7580–7590.
[33] a) Y. Zuo, X. Wang, Y. Yang, D. Huang, F. Yang, H. Shen, D. Wu, *Polym. Chem.* **2016**, *7*, 6432–6436; b) B. Li, T. He, X. Shen, D. Tang, S. Yin, *Polym. Chem.* **2019**, *10*, 796–818.
[34] H. Zhou, Q. Ye, X. Wu, J. Song, C. M. Cho, Y. Zong, B. Z. Tang, T. S. A. Hor, E. K. L. Yeow, J. Xu, *J. Mater. Chem. C* **2015**, *3*, 11874–11880.
[35] a) X. Wang, J. Zhang, Y. Wang, Y. Liu, Z. Li, Z. Xie, Z. Chen, *Adv. Funct. Mater.* **2017**, *27*, 1702051; b) X. Wei, M. Zhu, Z. Cheng, M. Lee, H. Yan, C. Lu, J. Xu, *Angew. Chem. Int. Ed.* **2019**, *58*, 1–6.
[36] a) Z. Xiang, C. Fang, S. Leng, D. Cao, *J. Mater. Chem. A* **2014**, *2*, 7662–7665; b) D. Kim, J. Kang, T. Wang, H. G. Ryu, J. M. Zuidema, J. Joo, M. Kim, Y. Huh, J. Jung, K. H. Ahn, K. H. Kim, M. J. Sailor, *Adv. Mater.* **2017**, *29*, 1703309; c) T. Gu, L. Cheng, F. Gong, J. Xu, X. Li, G. Han, Z. Liu, *ACS Appl. Mater. Interfaces* **2018**, *10*, 15494–15503.

Manuscript received: September 17, 2019
Revised manuscript received: October 13, 2019
Accepted manuscript online: October 14, 2019